J Sci Comput (2010) 45: 429–446
DOI 10.1007/s10915-010-9376-z

Pseudospectral Modeling of Nano-Optics in Ag Sphere Arrays

Bang-Yan Lin · Chun-Hao Teng · Hung-Chun Chang · Hui-Hsin Hsiao · Juen-Kai Wang · Yuh-Lin Wang

Received: 1 June 2009 / Revised: 7 March 2010 / Accepted: 11 May 2010 / Published online: 26 May 2010

Abstract We report a Legendre pseudospectral modeling of silver sphere arrays illuminated by light waves. A special feature of the present computation is that the dispersive nature of silver is described by a Drude-Lorentz model with model parameters obtained by fitting the frequency-domain complex-valued dielectric constants measured experimentally. Numerical validations are conducted based on solving both the near and far fields of the Mie scattering problem, and we observe good convergence on the numerical fields. The far-field patterns of the Ag sphere arrays are simulated. The results are compared to those obtained by the

A paper in memory of Prof. David Gottlieb.

This work is supported by National Science Council of Taiwan, grant No. NSC 96-2120-M-001-002.

B.-Y. Lin · H.-C. Chang
Graduate Institute of Communication Engineering, National Taiwan University, Taipei 10617, Taiwan

C.-H. Teng (✉)
Department of Applied Mathematics, National Chiao Tung University, Hsinchu 30010, Taiwan
e-mail: tengch@math.nctu.edu.tw

C.-H. Teng
Center of Mathematical Modeling and Scientific Computing, National Chiao Tung University, Hsinchu 30010, Taiwan

H.-C. Chang
Department of Electrical Engineering, National Taiwan University, Taipei 10617, Taiwan

H.-C. Chang · H.-H. Hsiao
Graduate Institute of Photonics and Optoelectronics, National Taiwan University, Taipei 10617, Taiwan

J.-K. Wang · Y.-L. Wang
Institute of Atomic and Molecular Science, Academia Sinica, Taipei 10617, Taiwan

J.-K. Wang
Center for Condensed Matter Sciences, National Taiwan University, Taipei 10617, Taiwan

Y.-L. Wang
Department of Physics, National Taiwan University, Taipei 10617, Taiwan

dipole-coupling-model method, and we observe very good agreement between these results. The near-field patterns are also computed, and localized enhanced electric fields in the inter-particle gap regions due to plasmonic coupling between Ag particles are visualized. As the gap between Ag particles is reduced the strength of the localized enhanced electric field is increased.

Keywords Pseudospectral simulation · Surface plasmon enhanced field · Plasmonic coupling · Ag nano-spheres

1 Introduction

Stable surface-enhanced Raman scattering (SERS) measurements have been demonstrated on metallic surfaces made of Ag nano-particle arrays embedded in anodic aluminum oxide substrates [26]. Such SERS substrates have important applications in rapid and accurate diagnosis for pathogens and their antibiotic susceptibility which is critical for controlling bacterial infections [21]. A key ingredient leading to these successful demonstrations is the plasmonic coupling between metallic nano-particles interacting with external light sources, which produces enhanced local field residing between adjacent Ag nano-particles. Thus, to fabricate SERS substrates which create desired optical properties it is important to have analytic and numerical tools to analyze the optical processes taking places on these substrates. Methods for computing the optical responses of particle arrays have been developed depending on the region of interest, far or near zone. For the far field, an approximation approach is the quasi-static dipole-coupling-model (DCM) [22] which has been used to study light scattering spectra from particles arrays [2]. The computed results consistently match the spectral properties observed in the SERS measurements [26]. For the near-field computations it is, however, not adequate to use the DCM method, since the particle geometry is simplified as a point and the wave dynamics occurring on the metallic surfaces of particles is neglected. To take these two factors into account, a feasible approach is by direct numerical simulations. For this purpose we present a numerical modeling framework for computing optical fields induced by such Ag nano-particle array based SERS substrates.

A glance on the physics of the underlying Ag nano-particle arrays is useful in prior of constructing a numerical scheme for simulating the optical field responses of the arrays. In this study two relevant issues are important. Firstly, since we are interested in the fields in the vicinity of Ag nano-particles, it is natural to consider a numerical approach which can accurately model geometries of the particles and capture the essential nature of waves crossing metal/dielectric interfaces described by the boundary conditions. The second issue is as follows. When incident light waves impinge upon the particles, each particle can be viewed as a cavity storing electromagnetic (EM) wave energy. At the same time, every particle also behaves as an antenna emitting energy out from itself. Notice that the emitted energy from a particle is partially radiated away from the array and partially stored in other particles again. So, it is expected that such a storing-and-radiating process takes a very long time for the entire stored energy to completely radiate out from the system. These requirements lead us to seek a numerical approach that can both accurately model boundary conditions enforced on possibly curvilinear metal-dielectric interfaces and preserve computing accuracy for long-time wave simulations.

Among EM wave simulation algorithms, the most popular and simple one is the second order accurate Cartesian finite difference time domain (FDTD) Yee method [23, 27]. However, the FDTD method may not be a suitable choice for the present study, because

in the simple FDTD framework, curved material boundaries are generally approximated by stair-cased interfaces and boundary conditions are not directly enforced. These simplified approaches may lead to inaccurate or possibly inconsistent computations [4]. Even with the use of local sub-grid method [23], which indeed improves the accuracy of the simulated fields near curved metallic-dielectric interfaces, the second order accurate FDTD method may not be an efficient method to preserve the numerical accuracy for the long-time wave evolutions, especially for multidimensional space wave problems, due to the accumulation of numerical dispersive error during long-time integration [18]. To resolve the above issues in EM wave simulations, high-order accurate element-wised computing methods have been developed, for instance, the discontinuous Galerkin finite element methods [11, 15, 16, 25] and the multidomain pseudospectral methods [24, 28–30]. These simulation schemes adopt flexible geometrical shape elements to well fit possible curved boundaries, and within each element high-order accurate computing algorithms with boundary conditions imposed properly are used to simulate EM fields. Due to their superior convergence performance, these schemes have lent themselves in various areas of EM applications such as designing low observable vehicles for military purposes (see [11] and references within [12]) and devising waveguide components for photonics applications [13, 16].

The physical and numerical issues mentioned above indicate that high-order accurate element-wised computational frameworks can be suitable methods to accurately analyze the optical responses of the aforementioned SERS substrates. Indeed, the use of high-order discontinuous Galerkin method for studying optical properties of Ag nano-wires has been successfully demonstrated [15]. Here, we illustrate a pseudospectral modeling of optics in nano-structures. The modeling is based on our previous established computational framework [24] for simulating EM waves propagating in regions filled with linear media. The framework is based on the Legendre pesudospectral penalty method [6, 7, 10] in space and Runge-Kutta discretization [3] in time, respectively, with hexahedron elements as building blocks. To simulate wave dynamics involving plasmon coupling induced by silver, we have to take the dispersive nature of the silver into account. A commonly used dispersive material formulation is based on the free electron Drude model. However, it will be shown later that the imaginary part of the complex-valued dielectric function in this model does not well fit those dielectric data measured experimentally [19] in the optical wavelength regime, especially around the plasmon resonant frequency. Thus, for broad-band gaussian wave excitations a more realistic dispersive model is needed. For this purpose, we propose a Drude-Lorentz model. The model parameters are obtained by fitting both the real and imaginary parts of the dielectric function to those realistically measured dielectric data. The model is then incorporated into the established pseudospectral computational framework though the auxiliary differential equation formulation [23].

Numerical experiments of the Mie scattering and Ag nano-sphere arrays impinged by light waves are performed to verify the performance of the computational setting. The numerical results obtained by the present method are compared to those obtained by the Mie series solution and the DCM approximation method. We see good agreements between the computed fields. Unfortunately, the divergence of the fields are not approximated very well, because the divergence laws and the material boundary conditions relating fields along the direction normal to material interface are not involved in the present formulation. This effect will be study in the future. Nevertheless, the good approximations on the field solution itself give us confidence that the present method can be used to compute optical fields in the vicinity of particle arrays. Because the scope of this paper is about the numerical performance of the computational framework, without losing generality, we limit ourself to the modeling of nano-optics in Ag sphere arrays with spheres packing in a square box configuration. For

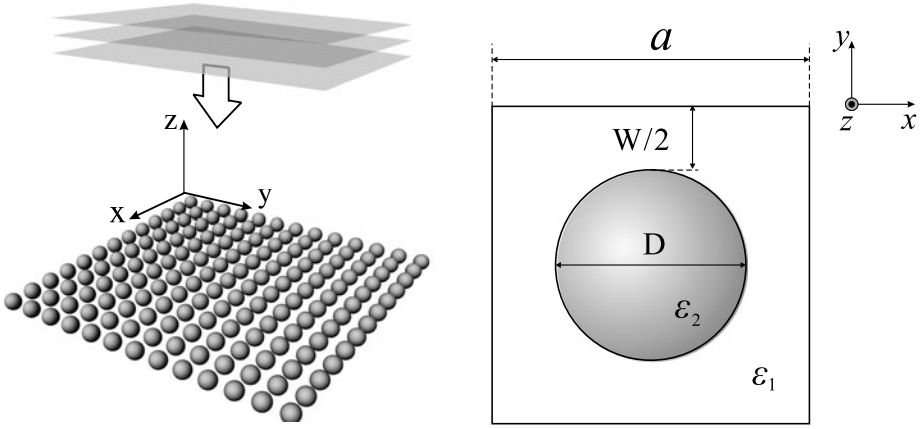

Fig. 1 *Left*: Periodically distributed nano sliver sphere array illuminated by plane waves from the top. *Right*: Top view of a unit cell of size $a \times a$ with a nano sphere of radius r placed at the center of the cell

simulation studies regarding the delicate EM physics on SERS based Ag nano-rods arrays [2, 26], we refer the reader to the work [20]. For the square box packing sphere arrays, the simulated near fields indicated that very strong localized enhanced electric fields take places around the sphere polar ends aligned parallel to the polarized direction of the electric incident waves. Moreover, the strength of the localized enhanced electric fields grows nonlinearly in the inter-particle gap regions as the inter-particle distance decreases.

The paper is organized as follows. In Sect. 2, the problem setting and its corresponding mathematical formulation are given. Issues related to the well-posedness of the problem are also discussed. Section 3 is devoted to the numerical formulation of the problem. Computational results and discussion are given in Sect. 4. Concluding remarks are given in Sect. 5.

2 Mathematical Formulation

2.1 The Physical Problem

Figure 1 shows a nano-particle array composed of a set of Ag spheres orderly distributed in a uniform simple background-medium, such as air. On the x-y plane the array system is composed of square cells of size $a \times a$, extended periodically along the x and y directions, with a Ag sphere of diameter D placed at the center of each cell. The distance between any two spheres is termed the gap size denoted by W. We are interested in the induced near- and far-field patterns of the system, illuminated by light waves from above. Since the system is periodically distributed in x and y directions, we thus only need to consider EM waves propagating within the square cylinder region formed by extending the area of a square cell along z-axis. Due to the periodicity of the structure, the EM fields on the parallel paired square cylinder walls perpendicular to the x-y plane are assumed identical.

2.2 Maxwell's Equations and Material Models

The EM fields within the square cylinder are described by the Maxwell equations:

$$\nabla \times \boldsymbol{H} = \frac{\partial \boldsymbol{D}}{\partial t} + \boldsymbol{J}, \qquad \nabla \times \boldsymbol{E} = -\frac{\partial \boldsymbol{B}}{\partial t}, \qquad \nabla \cdot \boldsymbol{D} = \rho, \qquad \nabla \cdot \boldsymbol{B} = 0,$$

where $\boldsymbol{E}$ and $\boldsymbol{H}$ are the electric and magnetic field strength functions, respectively, $\boldsymbol{D}$ and $\boldsymbol{B}$ are the electric and magnetic flux densities, respectively, and $\boldsymbol{J}$ and ρ are the electric current density and electric charge density functions, respectively. These field variables are functions of space time coordinates $(\boldsymbol{x}, t)$. To complete the formulation we need to specify constitution laws characterizing field behaviors in media. Note that both linear lossless and lossy dispersive metallic media are involved in this study. For the air background region, the medium is considered as linear and lossless. The constitution relationships relating the field variables are

$$\boldsymbol{D} = \varepsilon_0 \boldsymbol{E}, \qquad \boldsymbol{B} = \mu_0 \boldsymbol{H},$$

where ε_0 and μ_0 are the permittivity and permeability of air, respectively. The silver spheres are considered as dispersive media. The constitution relationships relating field variables are

$$\boldsymbol{D}(x,t) = \int_{-\infty}^{\infty} \varepsilon(\omega)\boldsymbol{E}(\boldsymbol{x},\omega)e^{-i\omega t}\,d\omega, \qquad \boldsymbol{B} = \mu_0 \boldsymbol{H},$$

where $\varepsilon(\omega)$ and $\boldsymbol{E}(\boldsymbol{x},\omega)$ are the dielectric function and electric field phasor in frequency domain, respectively.

Traditionally, the dielectric function $\varepsilon(\omega)$ for silver is formulated by the Drude model, and it takes the form

$$\varepsilon_D(\omega) = \varepsilon_\infty - \frac{\omega_p^2}{\omega(\omega + i/\tau)},$$

where ε_∞ is the high-frequency limit dielectric constant, ω_p is the plasma frequency, and τ is the relaxation time. In Fig. 2 the real and imaginary parts of the dielectric function of silver based on the Drude model parameters [5], are plotted for light wavelength from 0.2 μm to 1.1 μm. For comparison, the experimentally measured values of the complex dielectric constants of silver [19] are also sketched. It is shown that in the visible light regime the imaginary part of the Drude model based dielectric function does not fit the measured experimental data very well. To obtain a better modeling of the dielectric function, additional Lorentz terms are introduced into the model termed the Drude-Lorentz (DL) model. The dielectric function takes the form

$$\varepsilon_{\mathrm{DL}}(\omega) = \varepsilon_\infty - \frac{\omega_p^2}{\omega(\omega + i/\tau)} + \sum_{\alpha=1}^{k} \frac{f_\alpha \omega_p^2}{(\omega_\alpha^2 - \omega^2) - i\omega\Gamma_\alpha},$$

where ε_∞, ω_p and τ are as those in the Drude model, k is the total number of oscillators with frequency ω_α, strength f_α, and the damping constant Γ_α. The DL model used in this study contains two Lorentz oscillators, and the model parameters are obtained by curve-fitting the experimentally measured dielectric constants of sliver [19] through an optimization process summarized as follows. Define an object function

$$\Psi = \sum_j \left(\Re(\varepsilon_{\exp}(\omega_j) - \varepsilon_{\mathrm{DL}}(\omega_j))\right)^2 + \left(\Im(\varepsilon_{\exp}(\omega_j) - \varepsilon_{\mathrm{DL}}(\omega_j))\right)^2,$$

where $\varepsilon_{\exp}(\omega_j)$ and $\varepsilon_{\mathrm{DL}}(\omega_j)$ are the experimental data and the DL model based dielectric function values at the selected sampling frequencies ω_j, respectively. A set of optimized model parameters are determined by employing a genetic algorithm and a nonlinear least squares method alternatively. The values of these model parameters are given in Table 1. The constructed $\varepsilon_{\mathrm{DL}}(\omega)$ function is plotted in Fig. 2. A better agreement is shown between

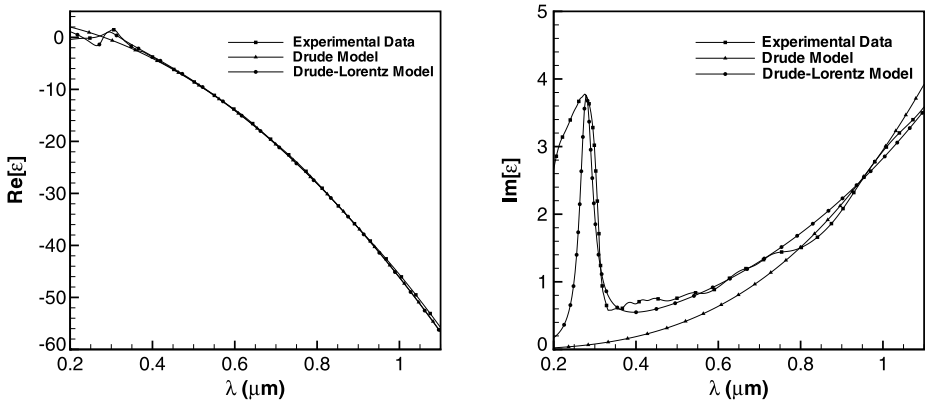

Fig. 2 Frequency-domain dielectric function ε of silver in the optical wavelength regime. *Left*: real part of ε. *Right*: imaginary part ε

Table 1 Parameters for the Drude-Lorentz model

ε_∞	ω_p (rad/s)	τ	f_1	ω_1 (rad/s)	Γ_1 (rad/s)
3.7	83996.63335E10	0.01485E-12	0.065	7793.80694E12	37116.08E12
			f_2	ω_2 (rad/s)	Γ_2 (rad/s)
			0.124	42502.97395E12	5730.73812E12

the experimental measured data and the model based constructed function, for the light wavelength beyond 0.3 μm.

2.3 Governing Equations and Boundary Conditions

The background-medium region is considered linear, lossless and source free, and we have the Maxwell equations in air as

$$\nabla \times \boldsymbol{H} = \varepsilon_0 \frac{\partial \boldsymbol{E}}{\partial t}, \qquad \nabla \times \boldsymbol{E} = -\mu_0 \frac{\partial \boldsymbol{H}}{\partial t}, \qquad \nabla \cdot \boldsymbol{E} = 0, \qquad \nabla \cdot \boldsymbol{H} = 0.$$

For the Ag particle region, the situation is more complicated. Recall that the dielectric function $\varepsilon_{\mathrm{DL}}(\omega)$ is a complex-valued function. To incorporate frequency-domain dielectric function $\varepsilon_{\mathrm{DL}}(\omega)$ into a time-domain framework, we adopt the auxiliary differential equation formulation [23]. The resulting governing equations for waves in a Ag particle region are

$$\nabla \times \boldsymbol{H} = \varepsilon_\infty \frac{\partial \boldsymbol{E}}{\partial t} + \sum_{\alpha=1}^{k} \frac{\partial \boldsymbol{P}_\alpha}{\partial t} + \boldsymbol{J}, \qquad \nabla \times \boldsymbol{E} = -\mu_0 \frac{\partial \boldsymbol{H}}{\partial t},$$

$$\nabla \cdot \boldsymbol{E} = -\frac{1}{\varepsilon_\infty} \sum_{\alpha=1}^{k} \nabla \cdot \boldsymbol{P}_\alpha, \qquad \nabla \cdot \boldsymbol{H} = 0,$$

$$\frac{\partial \boldsymbol{J}}{\partial t} + \tau^{-1} \boldsymbol{J} = \omega_p^2 \boldsymbol{E}, \qquad \frac{\partial^2 \boldsymbol{P}_\alpha}{\partial t^2} + \Gamma_\alpha \frac{\partial \boldsymbol{P}_\alpha}{\partial t} + \omega_\alpha^2 \boldsymbol{P}_\alpha = f_\alpha \omega_p^2 \boldsymbol{E},$$

where $\boldsymbol{P}$ and $\boldsymbol{J}$ are called the polarization and the electric current density, respectively.

We are interested in the responses of the Ag particles standing in air excited by an external light source with no fields in the domain initially. Thus, the initial conditions are $\boldsymbol{E} = 0$, $\boldsymbol{H} = 0$, $\boldsymbol{J} = 0$ and $\boldsymbol{P}_\alpha = 0$. On an air-Ag interface the boundary conditions relating the EM fields on both sides of the interface are needed. They are

$$\boldsymbol{n} \times \boldsymbol{E}_{\text{air}} = \boldsymbol{n} \times \boldsymbol{E}_{\text{Ag}}, \qquad \boldsymbol{n} \times \boldsymbol{H}_{\text{air}} = \boldsymbol{n} \times \boldsymbol{H}_{\text{Ag}},$$

along the direction tangent to the interface, and

$$\boldsymbol{n} \cdot \epsilon_0 \boldsymbol{E}_{\text{air}} = \boldsymbol{n} \cdot \left(\epsilon_\infty \boldsymbol{E}_{\text{Ag}} + \sum_{\alpha=1}^{k} \boldsymbol{P}_\alpha \right), \qquad \boldsymbol{n} \cdot \boldsymbol{H}_{\text{air}} = \boldsymbol{n} \cdot \boldsymbol{H}_{\text{Ag}},$$

along the direction normal to the interface. In the above expressions, $\boldsymbol{n}$ denotes the unit vector normal to the interface, and the subscripts air and Ag denote the regions, respectively.

Theoretically, to completely determine the EM fields one needs to find a solution satisfying the above complicated formulation, and this can be very challenging. In this study, by trading off the accuracy of the divergence fields we adopt an incomplete formulation which neglects the divergence equations and the normal direction boundary conditions, and we solve only the remaining time dependent equations subject to the initial conditions and the tangential boundary conditions. Since the incomplete formulation consists a linear hyperbolic system of equations, one can employ well established theory and simplifies the constructions of numerical schemes. We understand that this simplified formulation may cause a serious consequence that even with initial conditions satisfying the divergence equations exactly, the wave fields at later time may not satisfy the Gauss laws. The divergence free constraints are ruined is because that the normal direction boundary conditions on a material interface are not enforced. So, it can be expected that the divergence fields may not be modeled correctly on material interfaces. Indeed, from the numerical results which will be shown later, we observe that the approximated wave fields do not satisfy the divergence equations very well. Nevertheless, it is also shown from the simulations that the computed wave fields based on the simplified approach are still accurate enough to partially study the physics of the present problem. We admit that this issue concerning the divergence errors is important and it shall be studied in more details in the future.

We now state the problem in an initial boundary value format (IBVP). Introduce the state vectors

$$\boldsymbol{q}(\boldsymbol{x}, t) = (E_1, E_2, E_3, H_1, H_2, H_3)^T(\boldsymbol{x}, t), \qquad \boldsymbol{q}_J(\boldsymbol{x}, t) = (J_1, J_2, J_3, 0, 0, 0)^T(\boldsymbol{x}, t),$$

$$\boldsymbol{q}_\alpha(\boldsymbol{x}, t) = \left(\frac{\partial P_{1,\alpha}}{\partial t}, \frac{\partial P_{2,\alpha}}{\partial t}, \frac{\partial P_{3,\alpha}}{\partial t}, P_{1,\alpha}, P_{2,\alpha}, P_{3,\alpha} \right)^T (\boldsymbol{x}, t), \quad \alpha = 1, 2$$

and the notations

$$\mathbb{M}(u, v) = \begin{pmatrix} u\boldsymbol{I} & \boldsymbol{0} \\ \boldsymbol{0} & v\boldsymbol{I} \end{pmatrix}, \qquad \mathbb{A}_i = \begin{pmatrix} \boldsymbol{0} & \Delta_i \\ \Delta_i^T & \boldsymbol{0} \end{pmatrix}, \qquad \Delta_i = \begin{pmatrix} 0 & \delta_{i3} & -\delta_{i2} \\ -\delta_{i3} & 0 & \delta_{i1} \\ \delta_{i2} & -\delta_{i1} & 0 \end{pmatrix},$$

$$\mathbb{C}(u) = \begin{pmatrix} u\boldsymbol{I} & \boldsymbol{0} \\ \boldsymbol{0} & \boldsymbol{0} \end{pmatrix}, \qquad \mathbb{D}(\Gamma_\alpha, \omega_\alpha) = \begin{pmatrix} \Gamma_\alpha \boldsymbol{I} & \omega_\alpha^2 \boldsymbol{I} \\ -\boldsymbol{I} & \boldsymbol{0} \end{pmatrix},$$

where $\boldsymbol{I}$ and $\boldsymbol{0}$ are the identity and zero matrices of order 3×3, respectively, and δ_{ij} denotes the usual Kronecker delta function. Employing these notations we state the EM wave problem in the air region and in the metallic region as follows.

Air region (Ω_l):

$$\mathbb{M}(\varepsilon_0, \mu_0)\frac{\partial \boldsymbol{q}}{\partial t} + \sum_{i=1}^{3} \mathbb{A}_i \frac{\partial \boldsymbol{q}}{\partial x_i} = 0, \tag{1a}$$

$$\boldsymbol{q}(\boldsymbol{x}, 0) = \boldsymbol{f}_l(\boldsymbol{x}), \tag{1b}$$

$$\mathcal{B}_l \boldsymbol{q}(\boldsymbol{x}, t) = \boldsymbol{g}_l(\boldsymbol{x}, t) \quad \text{for } \boldsymbol{x} \in \delta\Omega_l, \tag{1c}$$

where $\delta\Omega_l$ denotes the boundary of the air region.
Ag particle region (Ω_d):

$$\mathbb{M}(\varepsilon_\infty, \mu_0)\frac{\partial \boldsymbol{q}}{\partial t} + \sum_{i=1}^{3} \mathbb{A}_i \frac{\partial \boldsymbol{q}}{\partial x_i} = -\mathbb{C}(1)(\boldsymbol{q}_J + \boldsymbol{q}_1 + \boldsymbol{q}_2), \tag{2a}$$

$$\frac{\partial \boldsymbol{q}_J}{\partial t} + \mathbb{C}(\tau^{-1})\boldsymbol{q}_J = \mathbb{C}\big(\omega_p^2\big)\boldsymbol{q}, \tag{2b}$$

$$\frac{\partial \boldsymbol{q}_\alpha}{\partial t} + \mathbb{D}(\Gamma_\alpha, \omega_\alpha)\boldsymbol{q}_\alpha = \mathbb{C}\big(f_\alpha \omega_p^2\big)\boldsymbol{q}, \quad \alpha = 1, 2, \tag{2c}$$

$$\boldsymbol{q}(\boldsymbol{x}, 0) = \boldsymbol{f}_d(\boldsymbol{x}), \qquad \boldsymbol{q}_J(\boldsymbol{x}, 0) = \boldsymbol{f}_J(\boldsymbol{x}), \qquad \boldsymbol{q}_\alpha(\boldsymbol{x}, 0) = \boldsymbol{f}_\alpha(\boldsymbol{x}), \tag{2d}$$

$$\mathcal{B}_d \boldsymbol{q}(\boldsymbol{x}, t) = \boldsymbol{g}_d(\boldsymbol{x}, t) \quad \text{for } \boldsymbol{x} \in \delta\Omega_d. \tag{2e}$$

Identifying boundary operators leading to the well-posedness of a problem is important in constructing a stable pseudospectral penalty scheme for solving the problem [10, 14]. To seek such well-posed boundary operators $\mathcal{B}_l$ and $\mathcal{B}_d$ for the IBVPs, we need to consider whether the IBVPs have bounded energy estimates. Since an energy estimate of the IBVP in the air region have been analyzed in [24] and the boundary operator $\mathcal{B}_l$ is found, we are left to find well-posed boundary operators for IBVP in the metallic region. Observe that (2) are coupled ordinary and partial differential equations. For well-posed analysis it is sufficient to consider whether the homogeneous version of the IBVP has a bounded energy estimate, since the ordinary differential equations (2b)–(2c) do not affect the well-posedness of the IBVP, provided that the homogeneous version of the IBVP is well-posed. This argument has been applied in analyzing the well-posedness for perfectly matched layer equations [1] for EM wave problems. Invoking this argument and neglecting the low-order terms in (2a)–(2c) we observe that the equations are decoupled. Notice that (1a) and (2a) are of the same form. Thus, taking $\mathcal{B}_d$ as same as $\mathcal{B}_l$ we conclude that the IBVP in the metallic region is also well-posed.

3 Pseudospectral Formulation

3.1 Legendre Pseudospectral Method

The Legendre pseudospectral method for approximating a function $f(\xi)$ defined on $\xi \in \mathsf{I} = [-1, 1]$ is based on constructing an N-th degree polynomial $f_N(\xi)$ of the form

$$f_N(\xi) = \sum_{j=0}^{N} l_j(\xi) f_j, \quad l_j(\xi) = -\frac{(1-\xi^2)P_N'(\xi)}{N(N+1)P_N(\xi_j)(\xi - \xi_j)}, \ f_j = f(\xi_j).$$

For $j = 0, 1, \ldots, N$, the distinct points ξ_j, termed the Legendre-Gauss-Lobatto (LGL) points, are roots of the polynomial $(1-\xi^2)P'_N(\xi)$ where $P_N(\xi)$ is the N-th degree Legendre polynomial and $'$ denotes the differentiation. The variables $l_j(\xi)$, $j = 0, 1, \ldots, N$, are the Lagrange interpolating functions based on the LGL grid points. The approximation of $f'(\xi_i)$ is achieved by differentiating f_N and then evaluating the resultant function values at the grid points, i.e.,

$$f'(\xi_i) \approx f'_N(\xi_i) = \sum_{j=0}^{N} l'_j(\xi_i) f_j.$$

For a three dimensional function $f(\boldsymbol{\xi})$, $\boldsymbol{\xi} = (\xi_1, \xi_2, \xi_3) \in \mathsf{I}^3$, the pseudospectral approximation method can be easily extended through the tensor product formulation. Let ξ_{1i}, ξ_{2j} and ξ_{3k} denote the N_1+1, N_2+1 and N_3+1 LGL grid points along ξ_1-, ξ_2- and ξ_3-axis, respectively. Then, the three dimensional grid points are defined as $\boldsymbol{\xi}_{ijk} = (\xi_{1i}, \xi_{2j}, \xi_{3k})$, $0 \le i \le N_1$, $0 \le j \le N_2$, $0 \le k \le N_3$. To approximate $f(\boldsymbol{\xi})$ we seek a polynomial $f_N(\boldsymbol{\xi})$ of the form

$$f_N(\boldsymbol{\xi}) = \sum_{ijk}^{N} \boldsymbol{L}_{ijk}(\boldsymbol{\xi}) f_{ijk}, \quad \boldsymbol{L}_{ijk}(\boldsymbol{\xi}) = l_i^{\xi_1}(\xi_1) l_j^{\xi_2}(\xi_2) l_k^{\xi_3}(\xi_3), \ f_{ijk} = f(\boldsymbol{\xi}_{ijk}),$$

where $\sum_{ijk}^{N} = \sum_{k=0}^{N_3} \sum_{j=0}^{N_2} \sum_{i=0}^{N_1}$, and $l_i^{\xi_1}(\xi_1)$, $l_j^{\xi_2}(\xi_2)$ and $l_k^{\xi_3}(\xi_3)$ are the one dimensional Lagrange interpolation functions based on the grid points ξ_{1i}, ξ_{2j} and ξ_{3k} distributed along the ξ_1-, ξ_2- and ξ_3-axis, respectively. The partial derivatives of $f(\boldsymbol{\xi})$ at the LGL grid points $\boldsymbol{\xi}_{pqr}$ are approximated as follows,

$$\frac{\partial f(\boldsymbol{\xi}_{pqr})}{\partial \xi_\nu} \approx \frac{\partial f_N(\boldsymbol{\xi}_{pqr})}{\partial \xi_\nu} = \sum_{ijk}^{N} \frac{\partial \boldsymbol{L}_{ijk}(\boldsymbol{\xi}_{pqr})}{\partial \xi_\nu} f_{ijk} \quad \text{for } \nu = 1, 2, 3.$$

3.2 Multi-domain Formulation and Maxwell's Equations in Curvilinear Coordinate

The present simulation study involves computing EM waves propagating in curved geometrical domains filled with heterogeneous media. To apply the pseudospectral method we decompose the global domain of interest into a union of non-overlapping hexahedral elements, possibly curvilinear, and within each element the material is considered homogeneous, i.e., the material parameters remain constant within a hexahedron. For each subdomain, we employ the transfinite blending function method [8, 9] to construct a one-to-one coordinate transformation, $\boldsymbol{\xi} = \Psi(\boldsymbol{x})$ and $\boldsymbol{x} = \Psi^{-1}(\boldsymbol{\xi})$, to map the element in the $\boldsymbol{x}$ coordinate onto the domain I^3 in the $\boldsymbol{\xi}$ space.

By utilizing the coordinate transformation and the chain rule of differentiation, (1)–(2) are rewritten as follows.

Air region:

$$\mathsf{M}(\varepsilon_0, \mu_0) \frac{\partial \mathsf{q}}{\partial t} + \sum_{\eta=1}^{3} \mathsf{A}_\eta \frac{\partial \mathsf{q}}{\partial \xi_\eta} = 0, \tag{3a}$$

$$\mathsf{q}(\boldsymbol{\xi}, 0) = \mathsf{f}_I(\boldsymbol{\xi}), \tag{3b}$$

$$\mathcal{B}_I^{\xi} \mathsf{q}(\boldsymbol{\xi}, t) = \mathsf{g}_I(\boldsymbol{\xi}, t) \quad \text{for } \boldsymbol{\xi} \in \delta \mathsf{I}^3. \tag{3c}$$

Ag particle region:

$$\mathsf{M}(\varepsilon_\infty,\mu_0)\frac{\partial \mathsf{q}}{\partial t}+\sum_{\eta=1}^{3}\mathsf{A}_\eta\frac{\partial \mathsf{q}}{\partial \xi_\eta}=-\mathsf{C}(1)(\mathsf{q}_J+\mathsf{q}_1+\mathsf{q}_2), \tag{4a}$$

$$\frac{\partial \mathsf{q}_J}{\partial t}+\mathsf{C}(\tau^{-1})\mathsf{q}_J=\mathsf{C}\big(\omega_p^2\big)\mathsf{q}, \tag{4b}$$

$$\frac{\partial \mathsf{q}_\alpha}{\partial t}+\mathsf{D}(\Gamma_\alpha,\omega_\alpha)\mathsf{q}_\alpha=\mathsf{C}\big(f_\alpha\omega_p^2\big)\mathsf{q},\quad \alpha=1,2, \tag{4c}$$

$$\mathsf{q}(\boldsymbol{\xi},0)=\mathsf{f}_d(\boldsymbol{\xi}),\qquad \mathsf{q}_J(\boldsymbol{\xi},0)=\mathsf{f}_J(\boldsymbol{\xi}),\qquad \mathsf{q}_\alpha(\boldsymbol{\xi},0)=\mathsf{f}_\alpha(\boldsymbol{\xi}), \tag{4d}$$

$$\mathcal{B}_d\boldsymbol{q}(\boldsymbol{\xi},t)=\boldsymbol{g}_d(\boldsymbol{\xi},t)\quad \text{for } \boldsymbol{\xi}\in\delta\mathrm{I}^3, \tag{4e}$$

where $\mathsf{q}(\boldsymbol{\xi},t)=\boldsymbol{q}(\boldsymbol{x}=\Psi^{-1}(\boldsymbol{\xi}),t)$ and likewise for the other field variables in serif font which are the transformed fields of those in the bold italic font in (1)–(2), and finally $\mathsf{M}=\mathbb{M}$, $\mathsf{A}_\eta=\sum_{\nu=1}^{3}\mathbb{A}_\eta\frac{\partial\xi_\eta}{\partial x_\nu}$, $\mathsf{C}=\mathbb{C}$ and $\mathsf{D}=\mathbb{D}$.

3.3 Pseudospectral Penalty Scheme

In our previous work [24] a multidomain pseudospectral penalty computational framework for simulating EM waves in linear medium has been established. To simulate optical responses of Ag sphere arrays, we incorporate the dispersive DL model into the framework. In what follows we present the numerical formulation for the dispersive metallic region only.

Denote the state vectors at the grid points by q_{ijk}, q^J_{ijk} and $\mathsf{q}^{L_\alpha}_{ijk}$. To numerically solve the set of (4) by the Legendre pseudospectral methods we seek numerical state vectors of the form

$$\mathsf{q}(\boldsymbol{\xi},t)=\sum_{ijk}^{N}\boldsymbol{L}_{ijk}(\boldsymbol{\xi})\mathsf{q}_{ijk}(t),\qquad \mathsf{q}_J(\boldsymbol{\xi},t)=\sum_{ijk}^{N}\boldsymbol{L}_{ijk}(\boldsymbol{\xi})\mathsf{q}^J_{ijk}(t),$$

$$\mathsf{q}_{L_\alpha}(\boldsymbol{\xi},t)=\sum_{ijk}^{N}\boldsymbol{L}_{ijk}(\boldsymbol{\xi})\mathsf{q}^{L_\alpha}_{ijk}(t),$$

which at the grid points satisfy the scheme

$$\mathsf{M}(\varepsilon_\infty,\mu_0)\frac{\partial \mathsf{q}_{ijk}}{\partial t}+\sum_{\eta=1}^{3}\mathsf{A}_\eta\frac{\partial \mathsf{q}_{ijk}}{\partial \xi_\eta}=-\mathsf{C}(1)\big(\mathsf{q}^J_{ijk}+\mathsf{q}^{L_1}_{ijk}+\mathsf{q}^{L_2}_{ijk}\big)-\frac{\sigma}{2}\mathsf{P}_{ijk}, \tag{5a}$$

$$\frac{\partial \mathsf{q}^J_{ijk}}{\partial t}+\mathsf{C}(\tau^{-1})\mathsf{q}^J_{ijk}=\mathsf{C}\big(\omega_p^2\big)\mathsf{q}_{ijk}, \tag{5b}$$

$$\frac{\partial \mathsf{q}^{L_\alpha}_{ijk}}{\partial t}+\mathsf{D}(\Gamma_\alpha,\omega_\alpha)\mathsf{q}^{L_\alpha}_{ijk}=\mathsf{C}\big(f_\alpha\omega_p^2\big)\mathsf{q}_{ijk},\quad \alpha=1,2, \tag{5c}$$

$$\mathsf{q}_{ijk}(0)=\mathsf{f}_d(\boldsymbol{\xi}_{ijk}),\qquad \mathsf{q}^J_{ijk}(0)=\mathsf{f}_J(\boldsymbol{\xi}_{ijk}),\qquad \mathsf{q}^{L_\alpha}_{ijk}(0)=\mathsf{f}_k(\boldsymbol{x}_{ijk}). \tag{5d}$$

We apply the penalty methodology which uses a free parameter σ and penalty terms P_{ijk} to weakly enforced the boundary conditions. These variables are determined such that the scheme is stable.

Similar to the well-posed analysis for the IBVP for the Ag particle region, the stability of the scheme (5) can be analyzed by conducting a discrete energy estimate for the homogeneous version of the scheme. By neglecting $\mathsf{C}(1)(\mathsf{q}^J_{ijk}+\mathsf{q}^{L_1}_{ijk}+\mathsf{q}^{L_2}_{ijk})$ in (5a) and the right hand side terms in the ordinary differential equations, (5a)–(5c) are then decoupled. We identify that the resultant homogeneous version of (5a) and the linear medium scheme shown in [24] are of the same form. Thus, the derived P_{ijk} and σ for the linear medium scheme [24] can be directly applied to (5) to ensure stable computations of waves in dispersive metallic media. For completeness, we give the expression of the penalty terms:

$$\begin{aligned}\mathsf{P}_{ijk} = {} & \frac{\delta_{0i}}{\omega_0^{\xi_1}}[\mathsf{SB}(\mathsf{R}-\mathsf{R}^{BC})]^{-\hat{\xi}_1}_{0jk} + \frac{\delta_{N_1 i}}{\omega_{N_1}^{\xi_1}}[\mathsf{SB}(\mathsf{R}-\mathsf{R}^{BC})]^{\hat{\xi}_1}_{N_1 jk} \\ & + \frac{\delta_{0j}}{\omega_0^{\xi_2}}[\mathsf{SB}(\mathsf{R}-\mathsf{R}^{BC})]^{-\hat{\xi}_2}_{i0k} + \frac{\delta_{N_2 j}}{\omega_{N_2}^{\xi_2}}[\mathsf{SB}(\mathsf{R}-\mathsf{R}^{BC})]^{\hat{\xi}_2}_{iN_2 k} \\ & + \frac{\delta_{0k}}{\omega_0^{\xi_3}}[\mathsf{SB}(\mathsf{R}-\mathsf{R}^{BC})]^{-\hat{\xi}_3}_{ij0} + \frac{\delta_{N_3 k}}{\omega_{N_3}^{\xi_3}}[\mathsf{SB}(\mathsf{R}-\mathsf{R}^{BC})]^{\hat{\xi}_3}_{ijN_3},\end{aligned}$$

where

$$[\mathsf{SB}(\mathsf{R}-\mathsf{R}^{BC})]^{-\hat{\xi}_1}_{0jk} = \mathsf{S}_{0jk}(-\hat{\xi}_1)\mathsf{B}_{0jk}(-\hat{\xi}_1)\big(\mathsf{R}_{0jk}(-\hat{\xi}_1) - \mathsf{R}^{BC}_{0jk}(-\hat{\xi}_1)\big)$$

and likewise for other parallel notations. The ω symbols are the LGL integration quadrature weights. The variables $\hat{\xi}_\nu$, for $\nu = 1, 2, 3$, are the unit vectors parallel to the ξ_ν axes, respectively. The variable $\mathsf{S}(\mathsf{n})$ is a unitary matrix which transforms the matrix A_η into a diagonal form, along the direction of a specified unit vector n. The matrix B is termed the numerical boundary operator. The symbol R is the characteristic state vector defined as $\mathsf{R} = \mathsf{S}^T\mathsf{q}$, and R^{BC} is the characteristic boundary condition to be imposed. The present penalty boundary condition imposition follows the concepts shown in [6, 7, 10, 14]. For the details of the derivations of P_{ijk} and the explicit expressions of the involved variables, we refer the reader to [24].

4 Numerical Results and Discussion

4.1 Validation

We use the Mie scattering of a dispersive metallic sphere as our first test example to valid the present simulation framework. The exact expressions of the Mie series coefficients can be found in [17]. Two sets of simulations are conducted for validations. The first set of simulations are conducted by using the Mie series solution as initial conditions and as supporting incident fields from the total-field-scattering-field (TFSF) interface [23]. The purpose is to examine whether the numerical solution converges as the degree of approximation polynomial N increases. For simplicity and without losing generality, we set $N_1 = N_2 = N_3 = N$. In Fig. 3, denoted by $\|\delta \boldsymbol{q}\|$, the L_∞-error of the state vector $\boldsymbol{q}$ (see [24] for the expression) as a function of time is plotted (dashed line). It is shown that the error decreases as N increases, indicating the convergence of the computational method. For the second set of simulations, we use vanishing fields as the initial condition, and a monochromatic plane wave with a raising gaussian profile as leading wavefront [24] is launched into the computational domain through the TFSF interface. We use the Mie solution as a reference. As time evolves

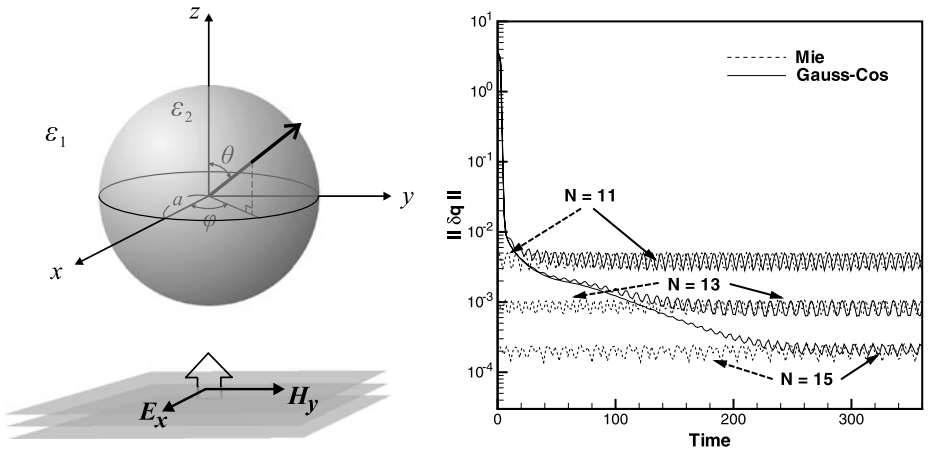

Fig. 3 *Left*: A schematic diagram of a metallic sphere illuminated by plane waves from below. *Right*: L_∞ error of Mie scattering of a metallic sphere

the difference between the computed and the reference solutions is measured (solid lines in Fig. 3). We see that for each given approximation polynomial degree N, the difference between the computed and the Mie solutions eventually reaches its corresponding approximation error level, indicating that the simulated fields have arrived at a periodic state in time within a desired accuracy.

It is interesting to point out that to obtain an accurate approximation to the metallic Mie scattering problem it requires a long-time evolution. In these numerical experiments, the external wave fields have magnitude of order one. In Fig. 3 we observe that for the computed solutions to arrive at an accurate periodic state in time a very long-time integration is required, for example, the computation with $N = 15$. This is not due to the inefficiency of the method. It is because the fields within the Ag spheres require a much longer time evolution to arrive at such an accurate periodic state. Because of this physical issue, to accurately simulate fields within the metallic region, it is better to use high-order methods such as the present method to preserve low numerical dispersion error during long-time computations.

We now present the numerical errors related to the divergence fields. Figure 4 shows the maximum values of the divergence errors of the EM fields within the metallic sphere. Notice that inside the metallic sphere, instead $\boldsymbol{E}$, it is the electric displacement field $\boldsymbol{D}$ that satisfies the divergence free constrains. The numerical experiments are conducted with initial fields provided by the Mie solution. It is shown that divergence errors are reduced as the degree of the approximation polynomial N increases, and the decreasing pattern of the divergence errors is similar to that of the error for the solution itself. However, it is clearly shown that the divergence errors are much larger than the solution error of the same N, indicating a poor convergence behavior on the divergence fields. From the limited computed results, we are unable to conclude if the divergence errors will further decrease to zero as N increases toward to infinity. There may be some non-zero divergence near or on the metallic boundary because the normal boundary conditions are not included in the present formulation. A detailed study of this effect is out of the scope of this paper and will be studied in the future.

For further validations, we use the scheme to compute the radar cross section (RCS) of a metallic sphere illuminated by a plane wave of wavelength λ. Denoted by σ_{3D} the RCS

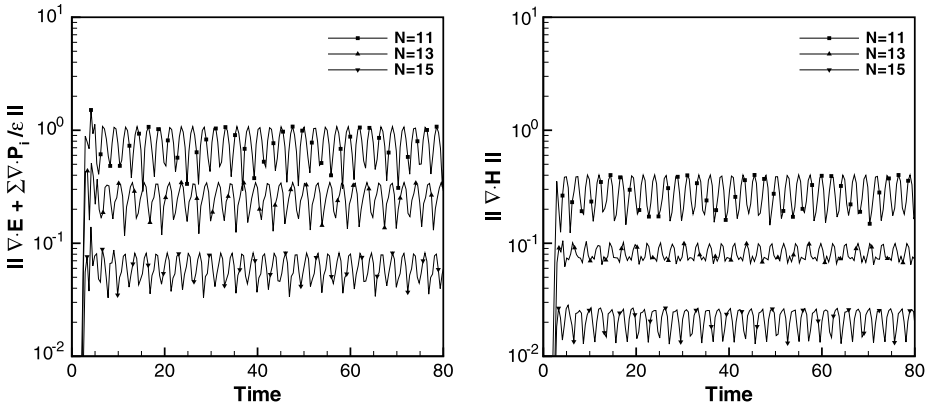

Fig. 4 Maximum values of $\nabla \cdot D$ and $\nabla \cdot H$ within a metallic sphere

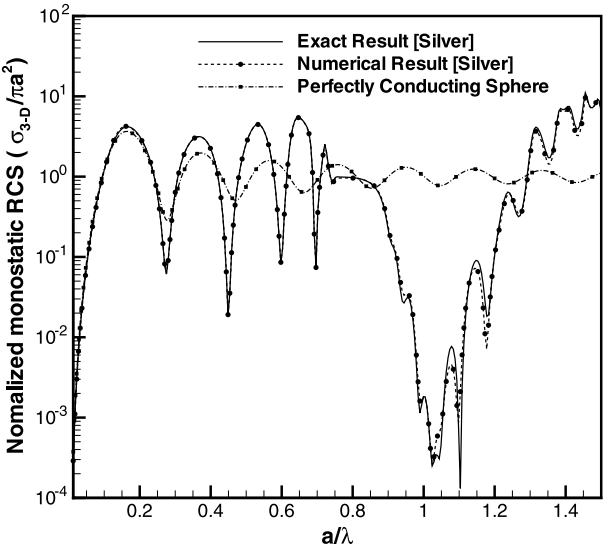

Fig. 5 Mono-static RCS of a metallic sphere and a perfectly conducting sphere. The exact result is referred to as the Mie series solution with dielectric constants provided by those experimentally measured values [19]. Computation parameters for the mono-static RCS computation: $\theta = \phi = \pi$. The results are normalized with respect to πa^2 where $a = 0.25$ μm

function is defined as

$$\sigma_{3D}(\lambda, \phi, \theta) = \lim_{r \to \infty} 4\pi r^2 \left| \frac{\boldsymbol{E}_s}{\boldsymbol{E}_{\text{inc}}} \right|^2,$$

where θ and ϕ characterize the position of the observation point at far-field, and $\boldsymbol{E}_{\text{inc}}$ as well as $\boldsymbol{E}_s$ represent the incident and scattering fields in frequency-domain, respectively. The RCS result is shown in Fig. 5, and we see that the numerical result agrees well with the exact one. For comparison, the RCS of an illuminated perfect electric conducting sphere of the same size is also plotted. We can see that the far-field scattering patterns resulting from the metallic sphere and the perfectly conducting one are obvious different, except in the Rayleigh scattering region ($a \leq 0.1\lambda$).

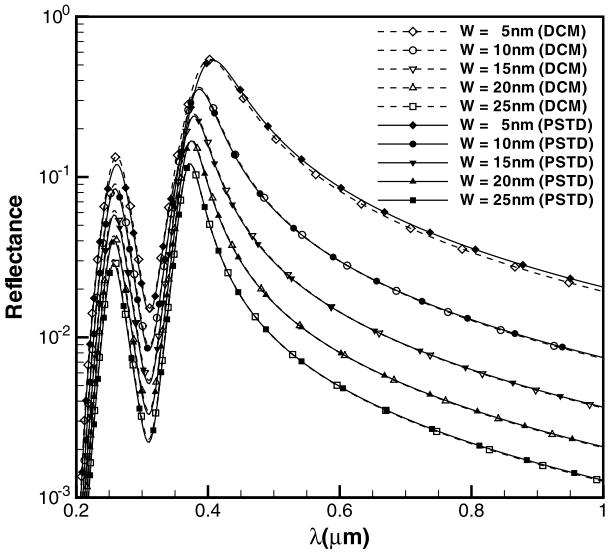

Fig. 6 Reflectance of Ag nano-sphere array computed by the dipole coupling model method and by the pseudospectral penalty scheme

4.2 Far-field Computations of Ag Sphere Arrays

We now turn our attention to the computations of optical fields induced by the Ag particle system excited by external light sources. To our best knowledge, we are unaware of any analytic methods to completely determine the fields for such a problem. However, if the illuminated Ag particles are considered as dipoles then the corresponding optical far-field patterns can be approximated by estimating the effective polarizabilities of the Ag particle array by the DCM method. It can be deduced from [22] that for an incident wave normally impinging upon the system the polarizability $\alpha_{\text{eff}}(\omega)$ is

$$\alpha_{\text{eff}}(\omega) = \frac{\alpha(\omega)}{1 - \frac{1}{2}\alpha(\omega)9.03/a^3}, \qquad \alpha(\omega) = \left(\frac{D}{2}\right)^3 \frac{\varepsilon(\omega) - 1}{\varepsilon(\omega) + 2}.$$

With c denoting the light speed in free space the reflectance $|r|^2$ relative to the polarizability is

$$|r|^2 = \left| \frac{A\alpha_{\text{eff}}(\omega)}{1 - A\alpha_{\text{eff}}(\omega)} \right|^2, \quad A = 2\pi\omega i c a^2,\ i = \sqrt{-1},$$

provided that the condition $k_0 a \ll 1$ holds, where k_0 is the free-space wave number of the incident wave and a is the lattice constance.

Notice that the reflectance is the energy ratio between the reflecting and incident waves, and it is equivalent to the observed monostatic RCS in the reverse direction of the incident light. Thus, we can make a comparison between the far-field results computed by the two methods. The computed reflectance and monostatic RCS are shown in Fig. 6, for arrays with different gap sizes. Indeed, we observe very good agreement between the results computed by the DCM and the present pseudospectral simulations. Besides, the red-shift pattern of the peak around the plasmon resonant frequency $\lambda = 400$ nm as the gap decreases, is qualitatively consistent with the experimental observations on the SERS substrates shown in [2].

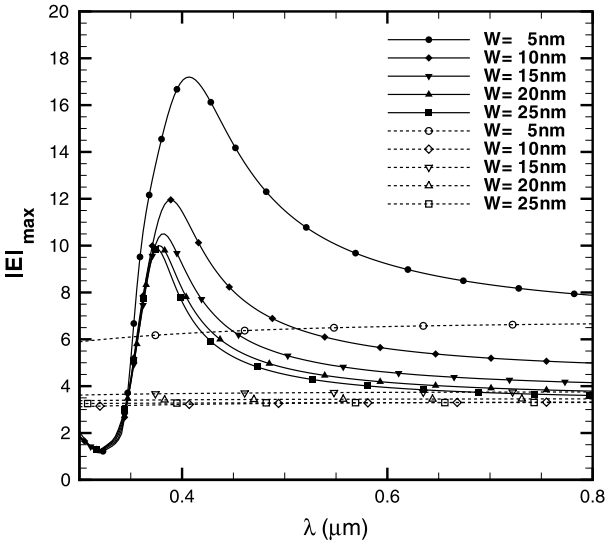

Fig. 7 Maximum values of the amplitude of $\boldsymbol{E}$ phasor field on the surface of a Ag sphere (*solid lines*) and a perfect electric conducting sphere (*dashed line*)

4.3 Near-field Computations of Ag Sphere Array

To investigate near-field patterns of Ag particle arrays by the DCM method may not be adequate because an illuminated Ag sphere is modeled by a dipole. As a consequence, the fields in the vicinity of a Ag sphere or the fields distributed on the spherical surfaces of Ag particles may not be calculated accurately. Since there are good agreements observed between the far-field results computed by the present numerical method and the DCM method, we are confident to use the numerical approach for further investigation on the near field responses of Ag nano-sphere arrays. For such a purpose, a gaussian type incident wave with its electric field polarized in the y-direction is lunched into the computational domain, and the wave is normally incident upon the system. The time-domain electrical and magnetic fields collocated at grid points on the upper hemispherical surface of a Ag sphere and on the x-y plane in the air region are collected till the fields in the computation domain fade away. The collected time-domain data are then converted through discrete Fourier transform in time to obtain the frequency-domain electric and magnetic phasor fields.

As a function of the incident light wavelength λ, the maximum value of the amplitude of the collected electric phasor field, denoted by $|\boldsymbol{E}|_{\max}$, is shown in Fig. 7, for different gap sizes. The simulations show that each $|\boldsymbol{E}|_{\max}$-λ curve is of a skewed gaussian shape, and it has a maximum value around $\lambda = 400$ nm. As the gap size decreases both the peak value and the bandwidth of the gaussian shape $|\boldsymbol{E}|_{\max}$-λ curve increase. The skewed gaussian shape peak is strongly related to the dispersive nature of silver, since we do not see such peaks if the Ag particles are replaced by perfect electrical conducting spheres. It is also seen that for a given gape size W the $|\boldsymbol{E}|_{\max}$-λ curves obtained from the dispersive and the perfectly electrical conducting particle systems, tend to merge together in the long wavelength region. This tendency indicates that when the incident light wavelength is much larger compared to the resonant wavelength the dispersive effect of the Ag particles becomes smaller, causing that the Ag particles behave like perfect electrical conducting ones. The calculations also indicate that an accurate dispersive model is needed in the optical wavelength regime in order to capture the essential EM wave responses from these Ag particles.

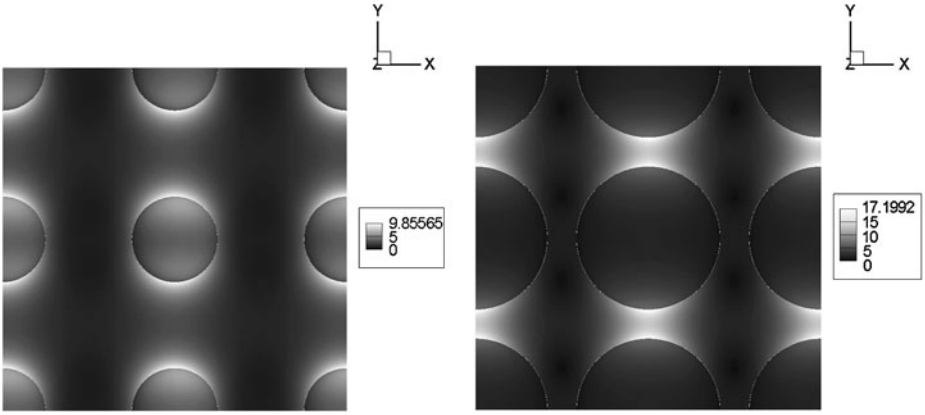

Fig. 8 The amplitude of $\boldsymbol{E}$ phasor field on the x-y plane and on the top hemisphere of Ag spheres for gap sizes $W = 25$ nm (*left*) and $W = 5$ nm (*right*)

Figure 8 shows the amplitude of the collected $\boldsymbol{E}$ phasor field plot of Ag sphere array with gap sizes $W = 5$ nm and $W = 25$ nm, illuminated by incident waves at the plasmon resonance wavelength ($\lambda \approx 400$ nm) with electric field polarized in the y-direction. We see that the $\boldsymbol{E}$ field near the two y-axis polar ends of a Ag sphere is enhanced locally. This is due to the fact that y-polarized incident waves drive the free electrons inside the Ag sphere to oscillate along the polarized direction, causing the enhancement to occur at those ends. For x-polarized incident waves, it is found that the localized enhanced field occurs near the two x-axis polar ends of a Ag sphere (not shown).

In Fig. 7 it is shown that around the plasmon resonance wavelength the peak value of the $|\boldsymbol{E}|_{\max}$-λ curve increases as the gap decreases, and the rate of increasing is nonlinear. In Fig. 8 it is observed that as the gap size is reduced the strength of the localized enhanced field is increased in the gap region. Such a nonlinear enhancement is resulting from the plasmonic coupling between any two Ag spheres. When the distance between two Ag spheres becomes smaller, the coupling between them becomes stronger. This leads to a stronger in-phase synchronization of the motions of free electrons inside any two Ag spheres. Such a synchronization extends the strength of the localized electric field in the gap region causing a stronger alignment of electrons in Ag spheres. As a positive feedback mechanism the two in-phase motions of electrons thus lead to a nonlinear enhancement of the $\boldsymbol{E}$ field around the polar ends of the sphere.

5 Concluding Remarks

In this paper, we report a multidomain pesudospectral modeling of nano-optics in Ag sphere arrays. A specific feature of the present computation is that in the Ag particle region a DL model based complex-valued permittivity function is used, where the model parameters are obtained by fitting permittivity function to those experimentally measured Ag dielectric constants in the optical wavelength regime. The computational framework is verified through the Mie scattering of a dispersive metallic scatterer impinged by optical waves. We observe a good convergence pattern on the solution itself. However, the divergence fields do not converge very well. The simulation results show that the divergence errors are much larger than the solution error for the same computational setting. It is suspected that such large

divergence errors are resulting from absence of the normal direction boundary conditions in the present formulation. This effect will be further study in the future.

In addition, the far-field patterns of Ag sphere arrays obtained by the present pseudospectral scheme and by the DCM method, are in good agreements. From the numerical simulations, we observe localized enhanced electric field around the two polar ends of Ag spheres. The results indicate that as the inter-particle distance is decreased the effect of plasmonic coupling between particles become stronger causing a nonlinear enhancement of the localized enhanced electric field near the two polar ends of Ag spheres.

We have seen both quantitatively and qualitatively agreements among the optical responses of Ag sphere arrays obtained by the present pseudospectral computational framework and by other analytic, approximation and experimental approaches. These agreements give us confidence that the present pseudospectral scheme can serve as an tool for studying fundamental physics underlining in more complicated SERS systems, such as Ag nanospheres or Ag nano-rods in different packing configurations, or even fully or partially embedded in SERS substrates. We will report such applications in the future.

Acknowledgement This work is supported by the National Science Council of Taiwan, grant No. NSC 96-2120-M-001-002.

References

1. Abarbenel, S., Gottlieb, D.: On the construction and analysis of absorbing layer in CEM. Appl. Numer. Math. **27**, 331–340 (1998)
2. Biring, S., Wang, H.-H., Wang, J.-K., Wang, Y.-L.: Light scattering from 2D arrays of mono-dispersed Ag nanoparticles seperated by tunable nano-gap: spectral evolution and analytic analysis of plasmonic couplig. Opt. Express **16**, 15312–15324 (2008)
3. Carpenter, M.H., Kennedy, C.A.: Fourth order 2N-storage Runge-Kutta scheme NASA-TM-109112, NASA Langley Research Center, VA (1994)
4. Ditkowski, A., Dridi, K., Hesthaven, J.S.: Convergent Cartesian grid methods for Maxwell's equations in complex geometries. J. Comput. Phys. **170**, 39–80 (2001)
5. Etchegoin, P.G., Ru, L.E.C.: Multipolar emission in the vicinity of metallic nanostructures. J. Phys.: Condens. Matter **18**, 1175–1188 (2006)
6. Funaro, D., Gottlieb, D.: A new method of imposing boundary conditions in pseudospectral approximations of hyperbolic equations. Math. Comput. **51**, 599–613 (1988)
7. Funaro, D., Gottlieb, D.: Convergence results for pseudospectral approximations of hyperbolic systems by a penalty-type boundary treatment. Math. Comput. **57**, 585–596 (1991)
8. Gordon, W.J., Hall, C.A.: Transfinite element methods: blending-function interpolation over arbitrary curved element domains. Numer. Math. **21**, 109–129 (1973)
9. Gordon, W.J., Hall, C.A.: Construction of curvilinear co-ordinate systems and applications to mesh generations. Int. J. Numer. Meth. Eng. **7**, 461–477 (1973)
10. Hesthaven, J.S.: Spectral penalty methods. Appl. Numer. Math. **33**, 23–41 (2000)
11. Hesthaven, J.S., Warburton, T.: Nodal high-order methods on unstructured grids. I. Time-domain solution of Maxwell's equations. J. Comput. Phys. **181**, 186–221 (2002)
12. Hesthaven, J.S., Warburton, T.: High-order accurate methods for time-domain electromagnetics. Comput. Model. Eng. Sci. **5**, 395–407 (2004)
13. Hesthaven, J.S., Dinesen, P.G., Lynov, J.P.: Spectral collocation time-domain modeling of diffractive optical elements. J. Comput. Phys. **155**, 287–306 (1999)
14. Hesthaven, J.S., Gottlieb, S., Gottlieb, D.: Spectral Methods for Time-Dependent Problems. Cambridge University Press, Cambridge (2007)
15. Ji, X., Cai, W., Zhang, P.: High-order DGTD methods for dispersive Maxwell's equations and modeling of silver nanowire coupling. Int. J. Numer. Methods Eng. **69**, 308–325 (2007)
16. Ji, X., Lu, T., Cai, W., Zhang, P.: Discontinuous Galerkin time domain (DGTD) methods for the study of 2-D waveguide coupled microring resonators. J. Lightwave Technol. **23**, 3864–3874 (2005)
17. Kong, J.A.: Electromagnetic Wave Theory. EMW Publishing, Cambridge (1999)
18. Kreiss, H.O., Oliger, J.: Comparison of accurate methods for the integration of hyperbolic equations. Tullus **24**, 199–215 (1972)

19. Lynch, D.W., Hunter, W.R.: Silver (Ag). In: Palik, E.D. (ed.) Handbook of Optical Constants of Solids, pp. 350–357. Academic, Orlando (1985)
20. Lin, B.Y., Hsu, H.C., Teng, C.H., Chang, H.C., Wang, J.K., Wang, Y.L.: Unraveling near-field origin of EM waves scattered from silver nanorod arrays using pseudo-spectral time-domain calculation. Opt. Express **17**, 14211–14228 (2009)
21. Liu, T.T., Lin, Y.H., Hung, C.S., Liu, T.J., Chen, Y., Huang, Y.C., Tsai, T.H., Wang, H.H., Wang, J.-K., Wang, Y.-L., Lin, C.H.: A high speed detection platform based on surface-enhanced Raman scattering for monitoring antibiotic-induced chemical changes in bacterial cell wall. Plos One **4**, e5470-1–e5470-10 (2009)
22. Persson, B.N.J., Liebsch, A.: Optical properties of two-dimensional systems of randomly distributed particles. Phys. Rev. B **28**, 4247–4254 (1983)
23. Taflove, A., Hagness, S.C.: Computational Electrodynamics: The Finite-Difference Time-Domain Method, 2nd edn. Artech House, Boston (2000)
24. Teng, C.H., Lin, B.Y., Chang, H.C., Hsu, H.C., Lin, C.N., Feng, K.A.: A Legendre pseudospectral penalty scheme for solving time-domain Maxwell's equations. J. Sci. Comput. **36**, 351–390 (2008)
25. Stannigel, K., Michael König, M., Niegemann, J., Busch, K.: Discontinuous Galerkin time-domain computations of metallic nanostructures. Opt. Express **17**, 14934–14947 (2009)
26. Wang, H.H., Liu, C.Y., Wu, S.B., Liu, N.Y., Peng, C.Y., Chan, T.H., Hsu, C.F., Wang, J.-K., Wang, Y.-L.: Highly Raman-ehhancing substrates based on silver nanoparticle arrays with tunable sub-10 nm gaps. Adv. Mater. **18**, 491–495 (2006)
27. Yee, K.S.: Numerical solution of initial boundary value problems involving Maxwell's equations in isotropic media. IEEE Trans. Antennas Propagat. **14**, 302–307 (1966)
28. Yang, B., Hesthaven, J.S.: A pseudospectral method for time-domain computation of EM scattering by bodies of revolution. IEEE Trans. Antennas Propagat. **47**, 132–141 (1999)
29. Yang, B., Hesthaven, J.S.: Multidomain pseudospectral computation of Maxwell's equations in 3-D general curvilinear coordinates. Appl. Numer. Math. **33**, 281–289 (2000)
30. Yang, B., Gottlieb, D., Hesthaven, J.S.: Spectral simulations of electromagnetic wave scattering. J. Comput. Phys. **134**, 216–230 (1997)